Journal of Power Sources 192 (2009) 200–207

Contents lists available at ScienceDirect

Journal of Power Sources

journal homepage: www.elsevier.com/locate/jpowsour

A 2D transient numerical model combining heat/mass transport effects in a tubular solid oxide fuel cell

Y. Mollayi Barzi*, M. Ghassemi, M.H. Hamedi

Department of Mechanical Engineering, K.N. Toosi University of Technology, Tehran, Iran

ARTICLE INFO

Article history:
Received 23 October 2008
Received in revised form 2 January 2009
Accepted 8 January 2009
Available online 19 January 2009

Keywords:
Dynamic simulation
Time response
Tubular SOFC
Load current
Numerical simulation

ABSTRACT

The purpose of this study is to present a 2D transient numerical model to predict the dynamic behavior of a tubular SOFC. In this model, the transient conservation equations (momentum, species and energy equations) are solved numerically and electrical and electrochemical outputs are calculated with an equivalent electrical circuit for the cell. The developed model determines the cell electrical and thermal responses to the variation of load current. Also it predicts the local EMF, state variables (pressure, temperature and species concentration) and cell performance for different cell load currents. Using this comprehensive model the dynamic behavior of Tubular SOFC is studied. First an initial steady state operating condition is set for the SOFC model and then the time response of the fuel cell to changes of some interested input parameters (like electrical load) is analyzed. The simulation starts when the cell is at the steady state in a specific output load. When the load step change takes place, the solution continues to reach to the new steady state condition. Then the cell transient behavior is analyzed. The results show that when the load current is stepped up, the output voltage decreases to a new steady state voltage in about 67 min.

1. Introduction

Solid oxide fuel cells (SOFCs) are a highly efficient, environmentally benign method of electric power production. SOFC systems have been proposed for electric utility power generation in both large central station power plants and distributed generation stations [1]. Considerable amounts of research work have been conducted to SOFC, making the SOFC close to the commercial applications. One of the challenges for application of SOFCs is their relatively slow response to the input parameters time variation. Understanding the transient behavior of SOFC's is also important for control of stationary utility generators during power system faults, surges, and switching. Therefore, the transient modeling of the fuel cell is useful to predict the cell dynamic behavior and operation. In 1994, Achenbach [2] analyzed the dynamic operation of a planar solid oxide fuel cell. He examined the transient cell voltage performance due to temperature changes and current density with lumped assumption for the cell temperature distribution. Hall and Colclaser [3] also developed a thermodynamic model for prediction of transient operation of the Tubular SOFC. Sedghisigarchi and Feliachi [4] combined heat transfer dynamics and species dynamics to form a new dynamic model. Also Xue et al. [5], considered a one-dimensional transient model for heat and mass transfer simulation assuming an electrical circuit include the Ohmic resistances and capacitors for the energy storage mode of operation. Iora et al. [6] considered the internal reforming/shifting reactions in fuel channel in their study. Qi et al. [7,8] developed a quasi 2D model of a tubular SOFC based on the changes along the gas flow direction using the control volume (CV) approach. In their model, the cell length is divided to several serial segments. Each segments includes five CVs, i.e. air tube, air channel (in two sections), cell body (electrolyte and electrodes) and fuel channel. They obtained a non-linear set of differential equations for the heat and mass transfer as well as electrical and electrochemical variables. By solving these equations simultaneously, they calculated the cell time response to the load change. One obvious weakness of these dynamic models is that they used constant heat and mass transfer coefficients based on a fully developed flow approximation at constant wall temperature and mass flux. In fact the tubular SOFC is a heat-generating tube with different flow streams on both the inner and outer side. We will avoid the fully developed flow approximation of Nusselt and Sherwood numbers at constant wall temperature/concentration in this 2D transient model by a complete field solution of the governing equations for the heat and mass transfer in the entire domain of a tubular SOFC working in a cell stack. Also the radial gradient of the state variables (i.e. temperature and species mole fractions) in air and fuel channels is predicted and therefore the time they need to diffuse in whole domain is taken in to account in present dynamic model.

* Corresponding author. Tel.: +98 21 44416906; fax: +98 21 44416906.
E-mail address: y_mollayi@dena.kntu.ac.ir (Y. Mollayi Barzi).

0378-7753/$ – see front matter © 2009 Elsevier B.V. All rights reserved.
doi:10.1016/j.jpowsour.2009.01.012

Nomenclature

A	surface area (m^2)
C_p	specific heat capacity ($J\,kg^{-1}\,k^{-1}$)
$D_{j,m}$	diffusion coefficient of jth species into the left gases of a mixture ($m^2\,s^{-1}$)
E	cell ideal voltage (V)
E_a	activation energy of anode ($J\,mol^{-1}$)
E_c	activation energy of cathode ($J\,mol^{-1}$)
F	Faraday's constant ($C\,mol^{-1}$)
G	Gibbs function ($J\,kg^{-1}$)
G^0	standard Gibbs function ($J\,kg^{-1}$)
T	temperature (K)
I	current (A)
i	current density ($A\,m^{-2}$)
k	pre-exponential factor ($A\,m^{-2}$)
$\dot{m}$	mass flux ($kg\,m^{-2}\,s^{-1}$)
M	molecular mass ($g\,mol^{-1}$)
n_e	number of electrons participating in electrochemical reaction
P	pressure (Pa)
$\dot{Q}$	volumetric heat source ($W\,m^{-3}$)
$\dot{q}$	heat source (W)
r	radius (m)
R	electrical resistance (Ω)
U	utilization percentage (0–1)
u	axial velocity ($m\,s^{-1}$)
v	radial velocity ($m\,s^{-1}$)
V	voltage (V)
X_j	jth species mol fraction
Y_j	jth species mass fraction

Greek symbols

η	electrical losses (V)
δ	thickness of layers (anode, cathode and electrolyte) (m)
ρ_p	electrodes and electrolyte electrical resistivity in node p ($\Omega\,m$)
θ	cell peripheral angel (rad)
ρ	density ($kg\,m^{-3}$)
μ	viscosity (Pa s)
λ	thermal conductivity ($W\,m^{-1}\,K^{-1}$)
ΔH	hydrogen heat value ($j\,mol^{-1}$)
$\Re$	universal gas constant ($J\,mol^{-1}\,K^{-1}$)
ΔV	volume of an element in the electrodes or electrolyte (m^3)

Subscripts

a	anode
c	cathode
e	electrolyte
act	related to activation loss
p	node p in the network circuit
Ω	related to Ohmic loss

2. Model description

2.1. Geometrical model

The computational domain and the flow streams of fuel and oxidant in a typical tubular SOFC is shown in Fig. 1. Due to symmetry, only half of the cell unit (between the cell symmetry axis and the symmetry line between two adjacent cells) is being analyzed. Fig. 2 shows the detailed view of the axi-symmetric computational domain and the cell overall heat and mass flows. As shown by the Figure, the computational domain includes the air and fuel channels, anode, cathode, electrolyte and the supporting tube layers. The fuel entrance is at the closed end of the cell. Table 1 presents the geometrical characteristics of the tubular SOFC [9,10]. The governing electrochemical, electrical as well as heat and mass transfer equations are as follows:

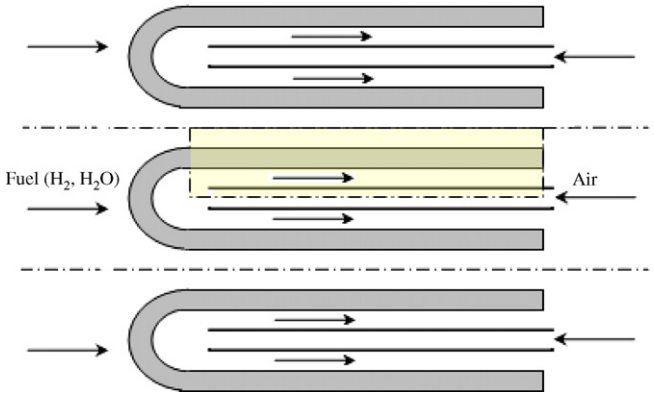

Fig. 1. The schematic diagram of a tubular SOFC and the computational domain.

2.2. Electrochemical model

The local ideal electromotive force (EMF) for the hydrogen electrochemical reaction is given by [12]:

$$E = \frac{-\Delta G}{n_e F} = \frac{-\Delta G^0}{2F} + \frac{\Re T}{2F} \ln \frac{(P_{O_2}/P^0)^{0.5}(P_{H_2}/P^0)}{P_{H_2O}/P^0} \quad (1)$$

where P^0 is the atmospheric pressure. Activation losses in anode and cathode of an elemental area (ΔA) are as follows, respectively [2]:

$$\eta_c = \frac{I}{\Delta A_c((4F/RT)k_c(P_{O_2}/P)^{0.25}\exp(-E_c/RT))} = R^c_{act} I \quad (2)$$

$$\eta_a = \frac{I}{\Delta A_a((4F/RT)k_a(P_{H_2}/P)^{0.25}\exp(-E_a/RT))} = R^a_{act} I \quad (3)$$

where P and T are local pressure and temperature, respectively. The hydrogen partial pressure is used in fuel channel while the oxygen partial pressure is considered in the air channel. The coefficients of Eqs. (2) and (3) are given in Table 2. The concentration polarization due to the non-uniform distribution of the species existing in the air and fuel flow passages is automatically taken into consideration by the mass transfer model, but the concentration polarization related to the diffusion of the species within the porous electrodes is ignored [3].

Table 1
Geometrical characteristics of the tubular SOFC unit [9].

	Thickness (μm)
Supporting tube	1500
Cathode	1000
Electrolyte	50
Anode	150
	Diameter (mm)
Inner side of air-inducing tube	8.0
Outer side of air-inducing tube	9.0
Inner side of supporting tube	13.8
Outer side of Anode	19.2
Outer diameter of fuel channel	29.2
	Length (mm)
Tubular cell unit	500

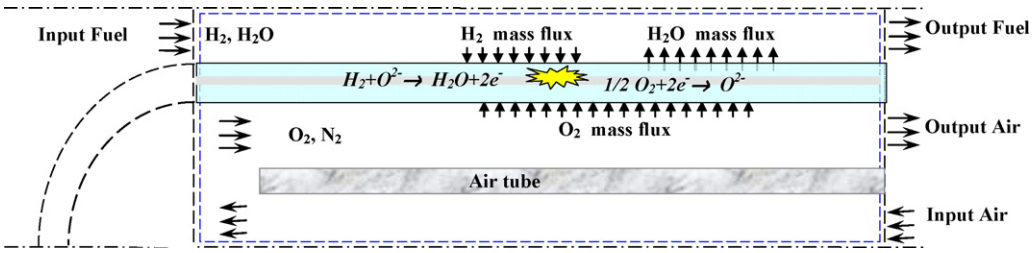

Fig. 2. Schematic of flow field in the computational domain.

Table 2
Coefficients of the activation polarization equation [11].

Coefficients	values
k_c	1.49×10^{10} A m^{-2}
k_a	2.13×10^{8} A m^{-2}
E_c	1.6×10^{5} J mol^{-1}
E_a	1.1×10^{5} J mol^{-1}

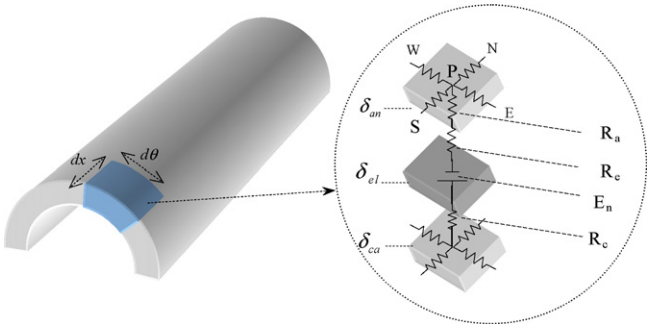

Fig. 3. Network circuit for a discretized element of the tubular SOFC.

2.3. Electrical model

Fig. 3 shows the equivalent network circuit for a discretized element of the tubular SOFC. The equivalent electrical circuit is used to calculate the cell current and voltage distribution in a specified load current. The circuit includes a set of electrical resistances and local electrical power sources. The schematic view of the overall equivalent circuit for half of the cell is depicted in Fig. 4. It should be noted that the interconnect resistances was neglected in compare with other resistances in the single cell. In order to calculate the current and voltage distribution in a specified load current, Kirchhoff's law is applied to each node. For each node, an equation associating the potential of the central grid point P in anode with the potentials of its neighboring points (east, west, north, and south) and also the corresponding grid P in the cathode is obtained. With all of the equations for the descritized grids in both the cathode and anode given, a matrix equation for potentials is created. The voltage in cathode connector is set to zero (as a reference voltage) and the total current taken out from the cell is prescribed. Then the potentials in each node and also in anode connector are calculated by solving the matrix of potential equations.

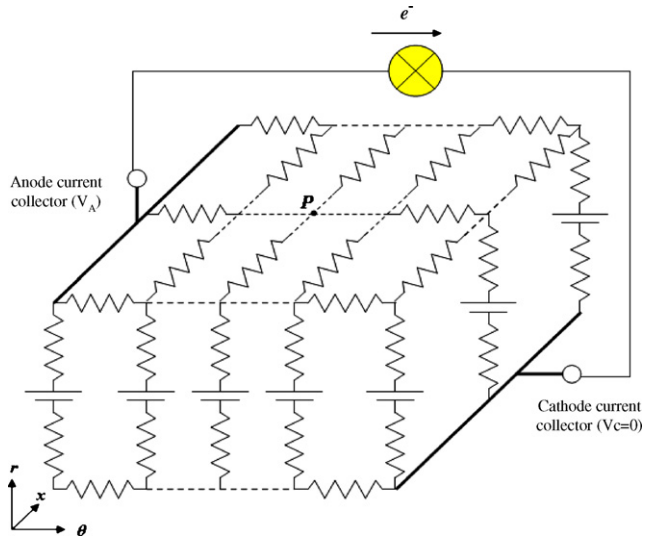

Fig. 4. Schematic view of the overall equivalent circuit for half of the cell.

The electrical resistances in radial direction for the anode, cathode and electrolyte are, respectively:

$$R_p^a = R_\Omega^a + R_{act}^a = \left(\frac{\delta_{an}\rho_p^a}{\Delta A_a}\right) + \left(\frac{1}{\Delta A_a((4F/RT)k_a(P_{H_2}/P)^{0.25}\exp(-E_a/RT))}\right) \quad (4)$$

$$R_p^c = R_\Omega^c + R_{act}^c = \left(\frac{\delta_c\rho_p^c}{\Delta A_c}\right) + \left(\frac{1}{\Delta A_c((4F/RT)k_c(P_{O_2}/P)^{0.25}\exp(-E_c/RT))}\right) \quad (5)$$

$$R_p^e = \frac{\delta_e\rho_p^e}{\Delta A_e} \quad (6)$$

ΔA is the average peripheral area of each element of electrodes or electrolyte and is $\Delta A = (r_{in} + r_{out}) \times d\theta \times dx/2$ (Fig. 3); where r_{in} and r_{out} are inner and outer radii of each layer, respectively. ρ_p is electrical resistivity of the cell material in node p, which is constant for the cathode and anode, but is temperature-dependent for the electrolyte, as it is given in Table 3 [11]. In Eqs. (4) and (5), P_{H_2} and P_{O_2} are partial pressures of H_2 and O_2 species at electrode–gas interfaces, respectively and T is the corresponding electrode temperature.

The longitudinal and peripheral resistances for the anode are calculated by, respectively:

$$R_{PE}^a = \frac{\rho_p^a r_a d\theta}{\delta_a dx} \quad (7)$$

$$R_{PN}^a = \frac{\rho_p^a dx}{\delta_a r_a d\theta} \quad (8)$$

The same set of relations (Eqs. (7) and (8)) is used for the cathode. The voltage difference between anode and cathode in any node is given by

$$V_p^a - V_p^c = E_p - (R_p^a + R_p^e + R_p^c)I_p \quad (9)$$

2.4. Heat and mass transfer model

To couple the flow and heat/mass transfer fields, a two-dimensional axi-symmetric computational domain is created (as

Table 3
Solid components properties of the cell [11].

Cell component	Thermal conductivity (W (m K)$^{-1}$)	Heat capacity (J (kg K)$^{-1}$)	Density (kg m^{-3})	Electrical resistivity (Ω m)
Cathode	6.0	623.0	4930.0	0.0186
Electrolyte	2.7	623.0	5710.0	0.3685 + 0.002838 exp(10300/T)
Anode	11.0	623.0	4460.0	0.0014
Supporting tube	1.1	623.0	4460.0	–
Air inducing tube	1.1	623.0	4320.0	–

shown in Fig. 2). Laminar flow assumption is used for the heat and mass transfer in air and fuel channels. This assumption is due to rather low flow velocity and Reynolds number (maximum 1000 in air channel) in both air and fuel channels [10,15]. Conservation equations are applied universally to entire computational domain, however zero velocities is assigned to solid area in the numerical treatment. The transient momentum, heat and mass transfer governing equations in cylindrical coordinate are used as follows, respectively:

$$\frac{\partial(\rho u)}{\partial t} + \frac{\partial(\rho u u)}{\partial x} + \frac{1}{r}\frac{\partial(r\rho v u)}{\partial r} = -\frac{\partial p}{\partial x} + \frac{\partial}{\partial x}\left(\mu\frac{\partial u}{\partial x}\right) + \frac{1}{r}\frac{\partial}{\partial r}\left(r\mu\frac{\partial u}{\partial r}\right) + \frac{\partial}{\partial x}\left(\mu\frac{\partial u}{\partial x}\right) + \frac{1}{r}\frac{\partial}{\partial r}\left(r\mu\frac{\partial v}{\partial x}\right) \quad (10)$$

$$\frac{\partial(\rho v)}{\partial t} + \frac{\partial(\rho u v)}{\partial x} + \frac{1}{r}\frac{\partial(r\rho v v)}{\partial r} = -\frac{\partial p}{\partial r} + \frac{\partial}{\partial x}\left(\mu\frac{\partial v}{\partial x}\right) + \frac{1}{r}\frac{\partial}{\partial r}\left(r\mu\frac{\partial v}{\partial r}\right) + \frac{\partial}{\partial x}\left(\mu\frac{\partial u}{\partial r}\right) + \frac{1}{r}\frac{\partial}{\partial r}\left(r\mu\frac{\partial v}{\partial r}\right) - \frac{2\mu v}{r^2} \quad (11)$$

$$\frac{\partial(\rho C_p T)}{\partial t} + \frac{\partial(\rho C_p u T)}{\partial x} + \frac{1}{r}\frac{\partial(r\rho C_p v T)}{\partial r} = \frac{\partial}{\partial x}\left(\lambda\frac{\partial T}{\partial x}\right) + \frac{1}{r}\frac{\partial}{\partial r}\left(r\lambda\frac{\partial T}{\partial r}\right) + \dot{Q} \quad (12)$$

$$\frac{\partial(\rho Y_j)}{\partial t} + \frac{\partial(\rho u Y_j)}{\partial x} + \frac{1}{r}\frac{\partial(r\rho v Y_j)}{\partial r} = \frac{\partial}{\partial x}\left(\rho D_{j,m}\frac{\partial Y_j}{\partial x}\right) + \frac{1}{r}\frac{\partial}{\partial r}\left(r\rho D_{j,m}\frac{\partial Y_j}{\partial r}\right) \quad (13)$$

In Eq. (12) the source term ($\dot{Q}$) is treated as follows:

In anode and cathode: the Joule volumetric heating source term due to Ohmic resistance and activation polarization is [11]:

$$\dot{Q}_p^a = \frac{R_p^a \cdot I_p^2}{\Delta V_p^a} \quad (14)$$

$$\dot{Q}_p^c = \frac{R_p^c \cdot I_p^2}{\Delta V_p^c} \quad (15)$$

In electrolyte: the Joule volumetric heating source term is due to Ohmic resistance:

$$\dot{Q}_p^e = \frac{R_p^e \cdot I_p^2}{\Delta V_p^e} \quad (16)$$

where ΔV_p is the volume of an element in the electrodes and electrolyte and is $\Delta V_p = \Delta A_p \times \delta$ and δ is the thickness of each layers.

In anode–electrolyte interface: the thermodynamic heat source is due to hydrogen electrochemical reaction [12]:

$$\dot{q}^{Th} = \left(\frac{\Delta H}{2F} - E_{n,p}\right) \cdot I_P \quad (17)$$

$E_{n,p}$ is the local Nernst voltage and I_p is the local current in node p.

The mass flux into/out of the fuel/anode boundary as well as air/cathode boundary is as follows, respectively:

$$\dot{m}_{H_2} - \dot{m}_{H_2O} = M_{H_2}\frac{i}{2F} - M_{H_2O}\frac{i}{2F} \quad (18)$$

$$\dot{m}_{O_2} = M_{O_2}\frac{i}{4F} \quad (19)$$

2.4.1. Physical and other properties

All transport and thermo-physical properties ρ, μ, C_p, λ and D_{ij} of the fuel and air are calculated as functions of the local temperature, pressure, and species concentrations. All the gaseous components are assumed to behave as perfect gases, and the local properties of the gas mixture are calculated according to the relations given in reference [16]. Table 3 gives the values used for heat conductivity, density and heat capacity and also the ionic and electric resistivities for the solid components [11].

2.4.2. Boundary conditions

The general boundary conditions for the computational domain (Fig. 2) are:

The inlet velocity of the fuel and air flow for a specified utility factor is given by [11]:

$$u_{fuel} = \left(\frac{A_{cell} i_{cell}}{2F U_{H_2} X_{H_2} A_{fuel}}\right)\frac{\Re T_{fuel}}{P_{fuel}} \quad (20)$$

$$u_{air} = \left(\frac{A_{cell} i_{cell}}{4F U_{O_2} X_{O_2} A_{air}}\right)\frac{\Re T_{air}}{P_{air}} \quad (21)$$

The species mass flux in air/cathode and fuel/anode interfaces (due to the local convection velocity and species mass diffusion) is as follows, respectively [11]:

$$\dot{m}_j^{air} = -D_{j,air}\rho_x^{air}\frac{\partial Yj}{\partial r} + \rho^{air} Y_j v_{air} \quad (22)$$

$$\dot{m}_j^{fuel} = -D_{j,fuel}\rho_x^{fuel}\frac{\partial Yj}{\partial r} + \rho^{fuel} Y_j v_f \quad (23)$$

where

$$v_{air} = \frac{\sum \dot{m}_j^{fuel}}{\rho} \quad (24)$$

and

$$v_{fuel} = \frac{\sum \dot{m}_j^{fuel}}{\rho} \quad (25)$$

The fuel exterior boundary (the boundary between adjacent cells) is assumed to be symmetrical.

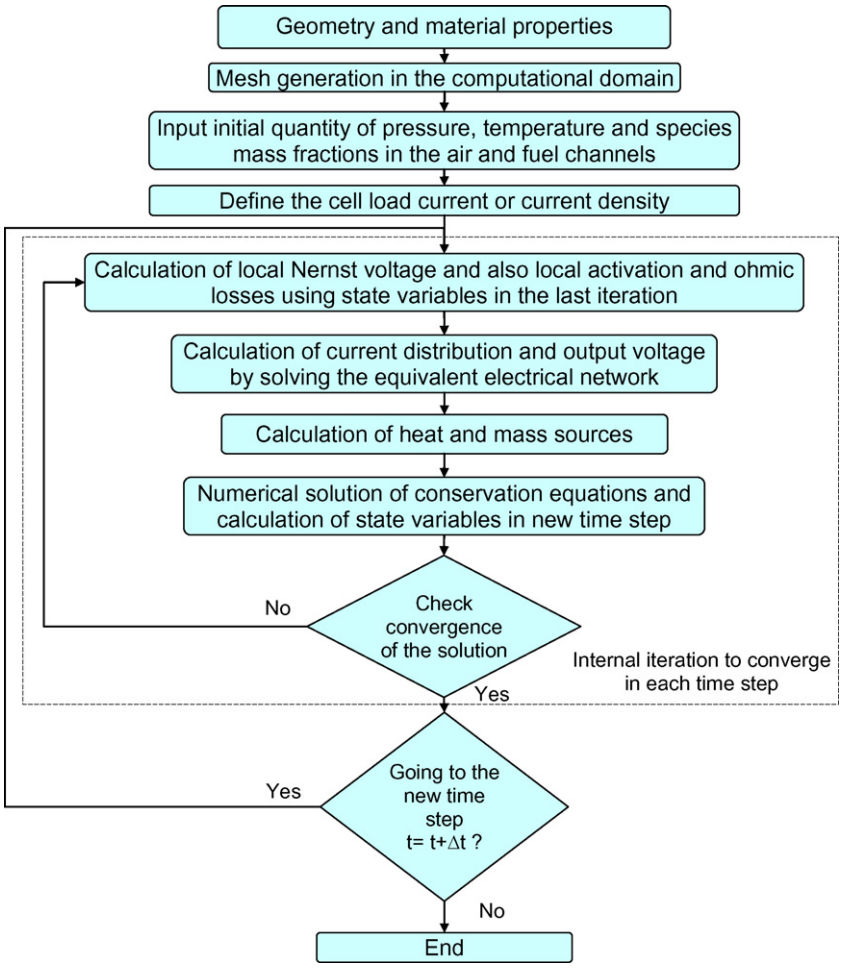

Fig. 5. Flowchart of the cell transient simulation process.

3. Simulation procedure of the cell transient operation

The flowchart for the overall simulation process of the cell transient operation is shown in Fig. 5. The simulation is based on a finite volume based code that uses separate modules for each sub-model (electrical, electrochemical and heat and mass transfer sub-models). The steady state solution of the cell is set as the initial value for the transient analysis. As shown in Fig. 5, at each time step an internal iteration is performed and continues until it converge. Then the code proceeds to the next time step utilizing previous results.

The governing transient transport equations (momentum, energy and species conservation equations) are solved by the SIMPLE algorithm. In this method the time steps do not affect the stability of the solution; however, it affects the accuracy of the results [13]. The computational domain is discretized by a 220×640 grid in radial and longitudinal directions, respectively. The grid independency of the results is examined and insured. The grids are uniform in longitudinal direction and non-uniform in the radial direction. This is due to very low thickness of the anode and electrolyte layers relative to the air and fuel channel width.

4. Results and discussion

For verification purpose, the current study polarization curve is compared to experimental data of Hagiwara et al. [14] and the steady state model of Li et al. [9] in Fig. 6. As shown the obtained results show good agreement, less than 0.25% deviation, with the experimental data especially for current density greater than 250 mA cm^{-2}. Results for current density less than 250 mA cm^{-2} show about 12% deviation with experimental data. This is due to the assumption and formulation of the activation and concentration polarization as well as the accuracy of numerical solution procedure. Furthermore, the present model results show less deviation from the experimental results than Li et al. results (about 5% more accurate). This is due to different treatment of the activation and

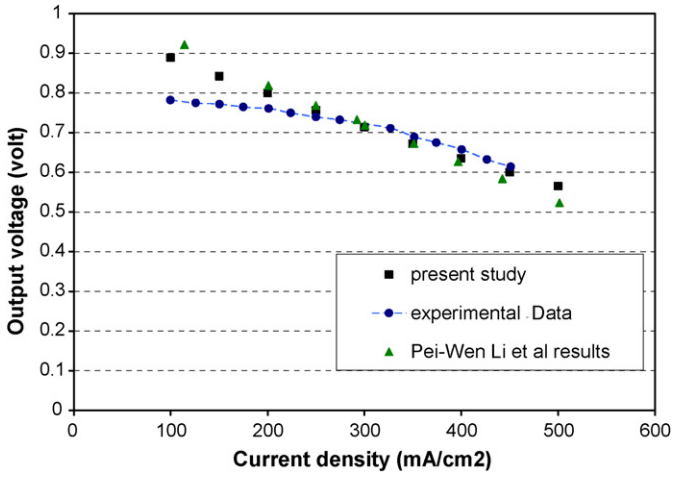

Fig. 6. Cell voltage versus current density.

Table 4
The cell operating conditions in steady state model [9].

Operating parameters	Values
The cell current density/output current	3500 A m^{-2}/104 A
Input air temperature	600 °C
Input fuel temperature	840 °C
Air and fuel pressure	1.013 atm
Input air composition	98% H_2, 2% H_2O
Hydrogen utility factor in fuel channel/fuel mass flow rate	0.85/0.00044 g s^{-1}
Oxygen utility factor in air channel/air mass flow rate	0.167/0.054 g s^{-1}

concentration losses in two models. They assumed the sum of the activation polarization and the concentration polarization occurring inside the porous electrodes is constant and is proportional to the electric current density. In general, it is well documented that sophisticated formulation and treatment of the activation and concentration loss causes more accurate simulation results.

4.1. Steady state results

The steady state operation results of the developed model are presented in this section. Input air and fuel conditions and also other setups of the cell for the steady state model are presented in Table 4. These steady state results are used as the initial values for the transient simulation.

Fig. 7 shows the cell temperature contours for load current density of 3500 A m^{-2}. The flow temperature rises downstream of the inlet and approaches to about 1000 °C due to the heat that is generated in the solid part and is conducted into the flow. Then temperature slightly decreases toward the cell closed end. Because the air that absorbs the major portion of the generated heat because of its higher mass flow rate. Therefore the radial temperature gradient in the air flow is more then the fuel flow. In the closed end region of the cell, non-uniformity of air temperature is reduced due to the mixing related to the flow recirculation there.

The relative pressure contours in air channel is depicted in Fig. 8. As shown by figure the pressure loss in air channel is calculated to be about 637 Pa. The input air gage pressure is set to 1280 Pa.

Fig. 9 shows the oxygen mass fraction contours in air channel. Diffusion of oxygen from the core region to the support tube surface

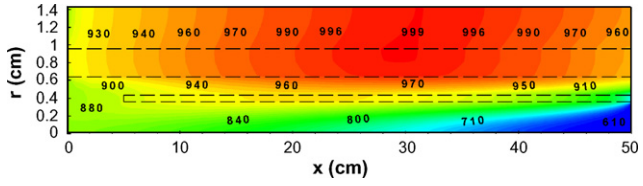

Fig. 7. Cell temperature contours (°C) in the whole computational domain.

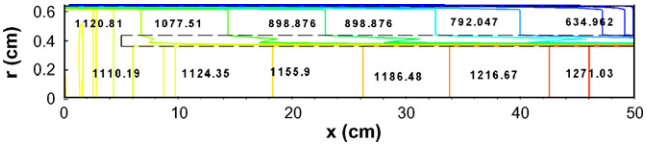

Fig. 8. Relative pressure contours (Pa) in the air channel with the input air gage pressure of 1280 Pa.

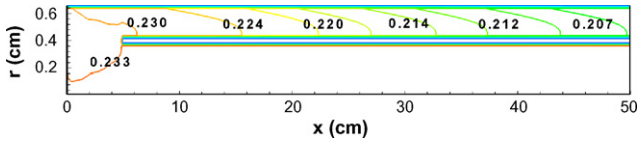

Fig. 9. Oxygen mass fraction contours in the air channel.

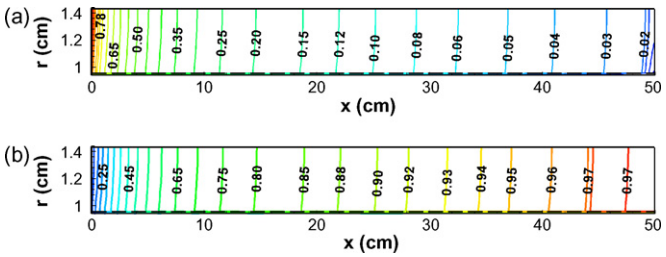

Fig. 10. Hydrogen and vapor mass fraction contours in the fuel channel.

forms a significant radial mass fraction gradient. As shown by the figure at the air tube outlet the oxygen mass fraction reaches to 0.207.

Fig. 10 shows the hydrogen and vapor mass fraction contours in the fuel channel. In the axial direction, the mass fraction of water vapor increases along the fuel channel from 0.13 up to 0.98, which is due to strong production rate of vapor from the anode wall. In the radial direction, water vapor and hydrogen concentrations do not show significant gradients. This is due to the strong diffusion of hydrogen in the fuel stream and very low fuel mass flow rate.

The flow streamlines in fuel and air channels are shown in Fig. 11. As shown the injected mass from the anode wall is comparable with the main mass flow in fuel channel. This is because of low mass flow rate of input fuel (due to high utility factor of hydrogen). However, in the air channel the consumed mass by the cathode wall is very low compared with the input air mass flow rate.

Fig. 12 shows the axial distribution of the cell local Nernst voltage and current density in the average load current density of 3500 A m^{-2}. Maximum Nernst voltage is about 1.13 V at the closed end of the cell where the fuel is coming in. in the inlet of the fuel the H_2 mass fraction is maximum and therefore Nernst potential is maximum there. Also current density decreases along the cell by decreasing the cell local voltage.

Generally the steady state results obtained from present dynamic model are in good agreement with the steady state models previously reported by Li et al. and also experimental data published by Hagiwara et al. [9,14].

4.2. Load change results

The simulation was conducted to determine the transient response of the cell to electrical load changes. The cell was subjected to a step increase in current density (from 1500 to 3500 A m^{-2}) with the fuel and air utility factors held constant. This means that the input fuel and air mass flow rates increases with load current increase.

Fig. 13 shows the axial temperature profiles of the cell during the transient operation up to steady state, for a step electrical load increase (from 1500 to 3500 A m^{-2}). As shown in figure, the temperature decreases at closed end side of the cell ($x < 0.18$ m) with an increase of load current but it increases at the air inlet side; however the maximum temperature decreases to about 1000 °C. Also the cell maximum temperature position shifts to the right hand side

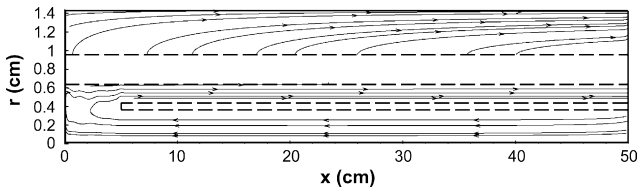

Fig. 11. The flow stream lines in fuel and air channels.

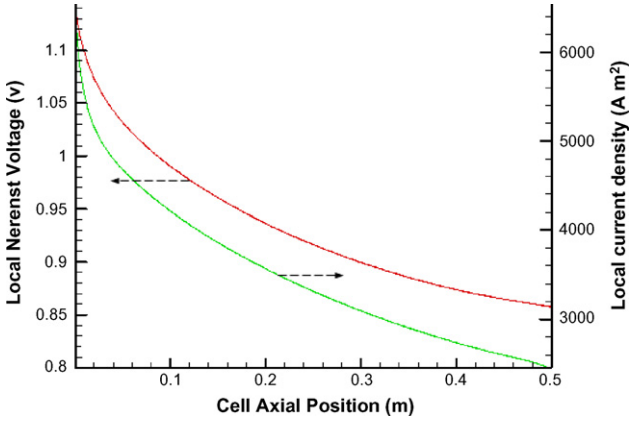

Fig. 12. Axial distribution of local Nernst voltage and current density in the load current density of 3500 A m^{-2}.

from 0.1 to 0.3 m (toward the air inlet throat). The reason is that the increase of the cell load current leads to increase of the air mass flow rate (about 130%) and its cooling effect, despite the increase of the electrochemical and electrical heat sources. Also maximum air-cooling effect takes place at the closed end of the cell and it absorbs maximum heat value from this region. However at the air inlet side, the increase of heat sources causes the increase of the cell body temperature because the air-cooling effect is less than thermal and electrical heating in this region.

Fig. 14 shows the cell closed end temperature history, under step external load change. As it can be seen in the figure the temperature decreases about 110 °C by increase of the load current. Also the time the cell temperature needs to reach to the new steady state condition (in current density of 3500 A m^{-2}) is calculated about 7000 s. However, the temperature response time obtained in present study is more than Hall et al. work (4500 s) [3]. It is due to the radial gradient of the state variables (i.e. temperature and species mole fraction) and the time they need to diffuse in whole domain. Also an over prediction of the solid–gas heat transfer coefficient can induce some errors in lumped or one-dimensional models.

The electrical transient response of the cell to the change in load current is depicted in Figs. 15–17. Fig. 15 represents the time history of the cell Nernst potential. As the external load current goes up from 1500 to 3500 A m^{-2}, the cell Nernst potential goes down from 0.934 to 0.926 V. it shows a fast response part (about 120 s) initially and then go back to new steady state value of 0.926 V during a slow transient response part (about 1 h in the current simulation). The transient response in the Nernst potential is very complex, which

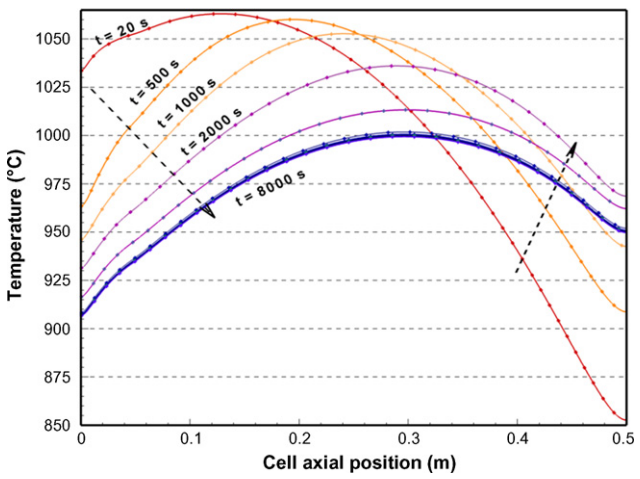

Fig. 13. The axial temperature profiles of the cell during transient operation.

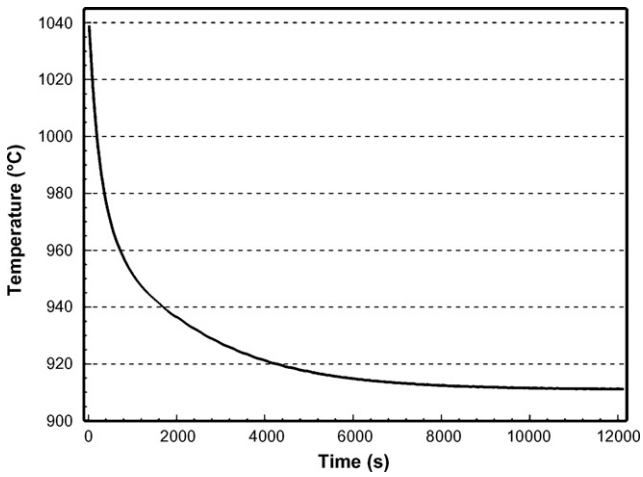

Fig. 14. The cell closed end temperature history under step external load change.

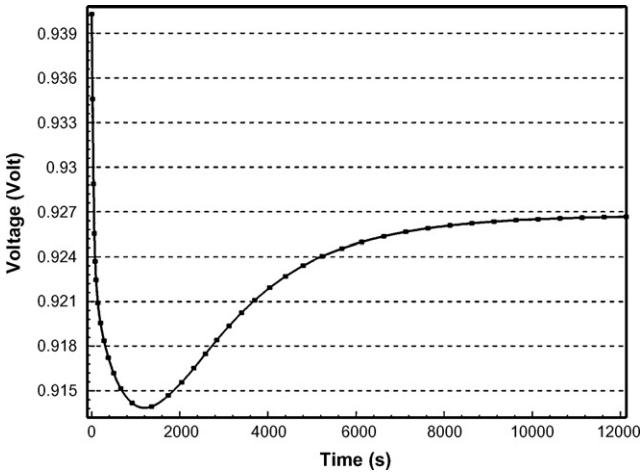

Fig. 15. Time history of the cell Nernst potential.

is related to all parametric changes associated with the entire fuel cell activity.

Fig. 16 shows the cell output voltage with time. After the load current experiences sudden change, the external load voltage goes down from 0.84 to 0.7 V initially and shows a very fast initial

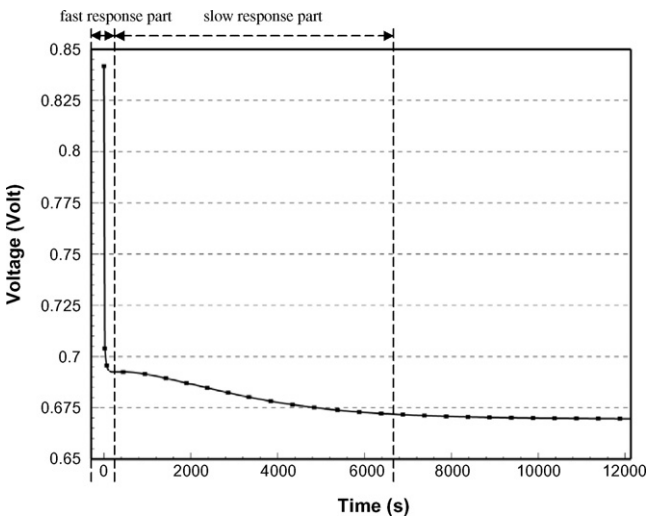

Fig. 16. The cell output voltage transient response to the change in load current.

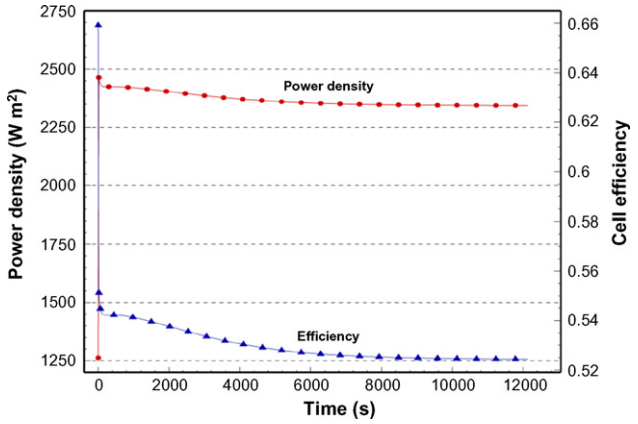

Fig. 17. The efficiency and power density history of cell under step external load change.

response. Then the voltage decays to the new steady state value (0.67 V) gradually, after about 67 min. this means that about 82% of voltage loss takes place in a very short time and other remain 18%, decreases during a very long time, about 67 min. it should be noted that because of very slow thermal response of the cell, the cell temperature distribution remains the same as before, at the first moment of the load change. Therefore the output voltage changes with the last temperature and species conditions initially. Then the temperature and species distribution reaches to the new steady condition associated with the entire fuel cell heat and mass sources and they affect the electrical parameters during a long time response (Fig. 16).

Fig. 17 depicts the efficiency and power density history of the fuel cell under step external load change. As shown in figure, the cell power density increases from 1250 to 2344 W m^{-2} when the external load current goes to 3500 A m^{-2}. It shows an overshoot of about 110% initially and then it decays back to the new steady state value. Also the cell efficiency decreases from 65% to about 52% after load change.

5. Conclusions

The newly developed 2D transient model provides the SOFC dynamic response to the cell electrical load change as well as the steady state operation. The conclusions drawn are as follows:

- The presented 2D model gives more realistic results than the previous one-dimensional and lumped models for the dynamic operation of the tubular SOFC, due to considering the *r*-direction gradients of the state variables (i.e. temperature and species mole fraction).
- When the load current is stepped up from 1500 to 3500 A m^{-2}, the output voltage decreases to 0.67 V after about 67 min.
- In a constant fuel and air utility factors, the cell maximum temperature decreases with increase of load current and it shifts toward the air inlet side.
- The inlet air mass flow rate and thermal and electrical heat sources are main parameters that determine the cell temperature distribution. The air-cooling effect in closed end of the cell is more than other places.
- The temperature and species concentration time response of the cell is very slow. It is calculated about 7000 s in studied case.
- Generally 82% of the cell electrical parameters variations take place just after the load change (very fast) and other remain 18% of variations is during a very long time relatively. This means that the effect of the cell temperature and species concentration on the electrical parameters time response is about 18% of the overall their variations.
- In longitudinal direction the mass fraction of vapor increases as well as the total fuel mass flow rate; while the oxygen mass fraction decreases.
- Radial non-uniformity of oxygen concentration in the air channel is noticeable so that the related concentration polarization is judged to be major. In contrast to this, the radial non-uniformity of the hydrogen concentration is not significant. Therefore, concentration polarization induced by the non-uniform distribution of species concentration in the flow space is not negligible at the cathode side but it can be ignored on the anode side.
- Pressure drop is about 640 Pa in the air channel while it is very low in fuel channel and can be neglected.

References

[1] K. Suzuki, H. Iwai, J.H. Kim, P.W. Li, K. Teshima, Proceedings of the 12th International Heat Transfer Conference, Grenoble, 2002, pp. 403–414.
[2] E. Achenbach, J. Power Sources 49 (1994) 333–348.
[3] D.J. Hall, R.G. Colclaser, IEEE Trans. Energy Convers. 14 (1999) 749–753.
[4] K. Sedghisigarchi, A. Feliachi, IEEE Trans. Energy Convers. 19 (2) (2004) 423–428.
[5] X. Xue, J. Tang, N. Sammes, Y. Du, J. Power Sources 142 (2005) 211–222.
[6] P. Iora, P. Aguiar, C.S. Adjiman, N.P. Brandon, Chem. Eng. Sci. 60 (2005) 2963–2975.
[7] Y. Qi, H.B. Luo, K.T. Chuang, J. Power Sources 150 (2005) 32–47.
[8] Y. Qi, B. Huang, J. Luo, J. Chem. Eng. Sci. 61 (2006) 6057–6076.
[9] P.W. Li, K. Suzuki, J. Electrochem. Soc. 151 (2004) A548–A557.
[10] P.W. Li, M.K. Chyu, J. Power Sources 124 (2003) 487–498.
[11] B. Sunden, M. Faghri, Transport Phenomena in Fuel Cells, Witpress, Boston, 2005.
[12] Y. Mollayi, M. Ghassemi, M.H. Hamedi, E. Afshari, Electrochem. Soc. Trans. 7 (2007) 1919–1925.
[13] S.V. Patankar, Numerical Heat Transfer and Fluid Flow, McGraw Hill, 1980.
[14] A. Hagiwara, H. Michibata, A. Kimura, M.P. Jaszcar, G.W. Tomlins, S.E. Veyo, Proceedings of the 3rd International Fuel Cell Conference, Nagoya, Japan, 1999, pp. 365–368.
[15] S. Campanari, P. Iora, J. Power Sources 132 (2004) 113–126.
[16] R.H. Perry, D.W. Green, J.O. Maloney, Perry's Chemical Engineers' Handbook, 7th ed., McGraw-Hill, New York, 1997.